Supersonic Performance of Disk-Gap-Band Parachutes Constrained to a 0-Degree Trim Angle

Anita Sengupta*

Jet Propulsion Laboratory, California Institute of Technology, Pasadena, California 91109

Richard Kelsch,[†] James Roeder,[‡] and Mark Wernet[§]

NASA John H. Glenn Research Center at Lewis Field, Cleveland, Ohio 44135

and

Allen Witkowski[¶] and Mike Kandis**

Pioneer Aerospace Corporation, South Windsor, Connecticut 06074

Supersonic wind-tunnel tests of 0.813 m disk-gap-band parachutes were conducted in a 10×10 ft cross section of a closed-loop wind tunnel. Four-percent-scale parachutes were attached to a 4%-scale Mars Science Laboratory (Viking-type) entry vehicle to simulate the free-flight configuration. The parachutes were tested from Mach 2 to 2.5 over a Reynolds number Re range of 2×10^5 to 1.3×10^6, representative of the Mars flight deployment envelope. A constrained parachute configuration was investigated to quantify the effect of parachute trim angle with respect to alignment with the entry-vehicle wake. In the constrained configuration, the parachutes were supported at the vent, using a rod that restricted parachute translation along a single axis. This was investigated for fixed trim angles of 0 and 10 degrees from the velocity vector. In the unconstrained configuration, the parachute was permitted to translate as well as trim and cone, in a manner similar to free flight. Nonintrusive test diagnostics were selected. An in-line load cell provided measurement of unsteady and mean parachute normal force. High-speed shadowgraph video of the upstream parachute flowfield was used to capture bow-shock motion and standoff distance. Stereo particle image velocimetry of the flowfield upstream of the parachute provided spatially resolved measurements of all three velocity components. Multiple high-speed-video views were used to document the supersonic inflation, parachute trim angle, projected area, and frequency of area oscillations. In addition, reflective targets placed in the interior of the canopy enabled photogrammetric reconstruction of the canopy-fabric motion (in both time and space) from the high-speed-video data.

Nomenclature

C_D	=	drag coefficient
D_o	=	nominal or constructed diameter
D_p	=	projected diameter
d	=	entry-vehicle diameter
F_D	=	axial drag force
$F_{D,RMS}$	=	axial rms drag
M	=	Mach number
m_p	=	parachute mass
q	=	freestream dynamic pressure
Re	=	Reynolds number
t	=	time
t_{FI}	=	time to full inflation
t^*	=	nondimensional inflation time
x/d	=	nondimensional trailing distance
v	=	freestream velocity
μ_p	=	mass ratio
ω_{AO}	=	area oscillation frequency

*Senior Engineer, Entry, Descent and Landing, Advanced Technologies, 4800 Oak Grove Drive, Mail Stop T1723-118. Senior Member AIAA.

†Aerospace Engineer, Applied Structural Mechanics Branch, 21000 Brookpark Road.

‡Mechanical Facility Engineer, Aeropower and Propulsion Test Engineering Branch, 21000 Brookpark Road.

§Senior Research Engineer, Optical Instrumentation, 21000 Brookpark Road. Associate Fellow AIAA.

¶Director Engineering Operations, 45 South Satellite Road. Member AIAA.

**Lead Engineering Analyst, 45 South Satellite Road. Member AIAA.

I. Introduction

THE Mars Science Laboratory (MSL) is NASA's next landed mission to the planet Mars. The mission will deliver to the surface NASA's most capable robotic geologist, an 850 kg laboratory equipped with an instrument suite to analyze the atmosphere and soil searching for carbon-based molecules and water, the building blocks of life. The science objectives of the mission necessitate access to landing sites 1 km above the gravitational equipotential reference surface and 60 deg from the equator. These landing sites also have a challenging surface terrain, including rocks as large as 0.5 m and a ground slope up to 15 deg [1]. These sites have previously been inaccessible due to limitations in the precision and capability of the entry, descent, and landing (EDL) system/phase of the Mars Exploration Rover, Phoenix, and Pathfinder missions [2]. The EDL phase of MSL is uniquely equipped, however, to meet these landing site challenges with a lifting-body trajectory from hypersonic entry to parachute deploy, active reaction control system control throughout the EDL sequence, supersonic parachute, propulsive descent, and tethered touchdown maneuver [3], yielding an error ellipse of 10 km from the designated surface target [4,5].

The parachute is a critical element of all Mars EDL systems, providing a mass- and volume-efficient source of aerodynamic drag. The parachute also provides the required difference in ballistic coefficients during the heat-shield and descent-vehicle separation events. During terminal descent, the parachute places the descent-vehicle (containing the Rover) at the appropriate velocity and altitude for a final propulsive descent with eight monopropellant hydrazine

thrusters. For reference, the descent vehicle is contained within the entry vehicle, also referred to as the aeroshell or entry vehicle. The MSL parachute is based on the Viking heritage disk-gap-band (DGB) design, originally developed in the 1970s to maximize drag and stability at supersonic speeds in low-dynamic-pressure environments [6]. The Viking program qualified a 16.1-m-nominal-diam DGB parachute over a range of supersonic low-dynamic-pressure deployments through a series of high-altitude balloon-launched rocket-assisted flight tests [7,8]. The Viking balloon-launched decelerator test (BLDT) essentially qualified the DGB parachute design for deployments up to 700 Pa and Mach 2.2 [9]. All NASA Mars missions since the Viking Lander have flown DGBs less than 16 m in diameter and deployed at less than Mach 2, enabling them to take advantage of the existing supersonic qualification and eliminating the need for a prohibitively expensive high-altitude test program [10]. MSL presents a departure from the existing heritage argument, however, as it will fly a 21.5 m DGB and deploy at up to 750 Pa and Mach 2.3, making it the largest, fastest, and highest-opening-load DGB parachute ever to be deployed on Mars (or Earth).

The aforementioned MSL parachute size and deployment conditions were selected to provide the drag, ballistic coefficient, and terminal velocity to achieve the EDL timeline and also to provide geometric, aerodynamic, and trajectory similarity to the Viking BLDT qualification flights [8]. However, this trajectory will subject the parachute to up to 10 s of operation above Mach 1.5. This is an area of concern, as DGB parachutes tested supersonically from the Viking and pre-Viking era have been observed to exhibit a supersonic instability between Mach 1.5 and 2.5 [11–13]. The instability is characterized by periodic infolds in the band, leading to localized fabric collapse and subsequent reinflation. Each reinflation event subjects the parachute to a load on the order of the opening load. This phenomenon is commonly referred to as *area oscillations* and results in unsteady drag coincident with shape and lateral instability. Recent experimental work with a 0.46-m-nominal-diam rigid DGB parachute has shown that the instability is driven by aerodynamic coupling of the parachute bow shock and forebody wake and is dependent on Mach and Reynolds numbers and proximity to and shape of the forebody [14]. However, the dynamic response of the parachute during the instability is not understood.

Area oscillations introduce uncertainties in the modeling of the descent phase of the mission as well as the potential for dynamics of the entry vehicle under the parachute. Of additional concern is the difficulty in quantifying the dynamic loading that the parachute will experience due to this instability and how this might affect the parachute's structural integrity due to self-abrasion and repeated loading events. In the absence of a full-scale supersonic qualification test, quantification of this phenomenon is needed. Specifically, the aerodynamic, geometric, and scale dependence of the area oscillation should be determined.

Supersonic wind-tunnel tests of 4%-scale MSL parachutes were conducted in support of the MSL parachute development and qualification. These tests investigated the aerodynamic coupling of the entry-vehicle wake to the parachute flowfield to determine the cause and functional dependence of supersonic area oscillations. Results were used to determine the frequency of the instability and the dynamic drag variation and to provide an update to the Mach efficiency curve for Viking-type DGB parachutes from Mach 2.0 to 2.5. The test program was also designed to generate a validation data set for fluid–structure-interaction computational tools under development for MSL [14,15]. The flexible test program is based on a prior CFD validation experiment that explored the aerodynamics of a 2.1% rigid MSL parachute with entry vehicle [14].

II. Experimental Setup

A. Wind-Tunnel Test Configuration

The 4%-scale parachute test was conducted in a closed-loop supersonic wind tunnel. The test section has a $10 \times 10 \times 40$ ft ($0.021 \times 0.021 \times 0.85$ m) geometry with smooth walls. Mach number is controlled with flexible-wall nozzle geometry that provides Mach 2 to 3.5 airflow velocity and is calibrated to be within ± 0.01 Mach and ± 0.25 deg flow angularity. An exhaust system enables variable pressure operation from 1 to 35 kPa dynamic pressure, providing a Reynolds number range of 3.94×10^5 to $1.12 \times 10^7/$m [16].

A schematic of the test configuration is shown in Fig. 1. Four-percent scale was the maximum-size parachute (0.55 m projected diameter) that could be used without having reflected shocks (from the entry vehicle) interfere with the parachute flowfield. This is essential to preserving the flightlike nature of the entry-vehicle–wake interaction. A swept-back diamond-wedge stainless steel strut was selected to mount the entry vehicle to the tunnel. The entry vehicle is a 4% representation of the MSL 70 deg sphere-cone forebody with biconic backshell, similar to the Viking configuration [17]. It is mounted at 0 deg angle of attack relative to the freestream velocity vector. The strut provides minimum aerodynamic interference along with sufficient stiffness to prevent entry-vehicle vibration. It was designed to a maximum parachute inflation load of 13.3 kN at a 16 deg trim angle. In both test configurations, the parachute was attached to the entry vehicle via a single-axis load cell, as shown in Fig. 2. The load cell was hard-mounted to the inside of the entry vehicle, and a flexible Kevlar riser was used to connect it to a swivel, which afforded the parachute system three rotational and three translational degrees of freedom in the unconstrained configuration.
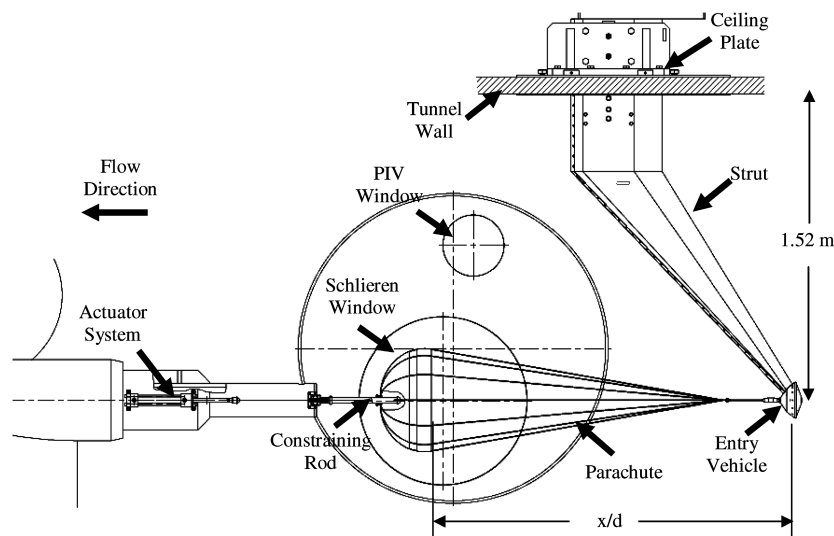

Fig. 1 Schematic of the parachute with entry-vehicle test configuration in the supersonic wind tunnel.

A second Kevlar riser was used to attach the swivel to the parachute suspension lines through a multibridle. All of the textile-to-metallic component connections were sized to provide an axial trailing-distance ratio x/d of 10.6. This ratio is defined as the axial distance from the parachute's leading edge to the entry-vehicle maximum diameter divided by the entry-vehicle maximum diameter. A schematic of the constrained parachute is shown in Fig. 3. The parachute was maintained at a 0 deg trim angle in relation to the entry vehicle and freestream direction by a constraining rod that passed through the apex of the parachute. This allowed the parachute to rotate freely and translate axially along the constraining rod, but prohibited all other degrees of freedom.

The test matrix is shown in Table 1. Test conditions were chosen to match the Mach and Reynolds numbers of the MSL deployment envelope. CFD analyses suggest that the supersonic parachute instability under investigation is dependent on Reynolds number and Mach number [18]. To match the Reynolds number on Mars, the test dynamic pressure is significantly higher than the flight value.

The test section has multiple windows for optical access. A pair of 84-cm-diam optical-grade windows were used for shadowgraph videography of the flowfield around the canopy. Two 30 cm windows located just above the schlieren windows provided access for the particle image velocimetry (PIV) cameras. The PIV laser sheet was fed through a 13 cm window in the tunnel test-section floor, which provided a streamwise plane upstream of the parachute from an x/d of 6 to 10. Two 84 cm windows upstream of the entry vehicle were used for high-speed-video cameras and lighting. Two additional windows in the floor and ceiling upstream of the entry vehicle provided vantage points for high-speed-video footage of the parachute from the floor and ceiling.

B. Subscale Parachutes

The subscale test articles were 4%-scale of the full-scale parachute based upon the nominal diameter or the constructed diameter. Table 2 documents the relevant dimensions, material properties, and non-dimensional scaling parameters of the subscale test articles as compared with the full scale. A schematic of the subscale parachute is shown in Fig. 4. The subscale articles are geometrically scaled from the standard Viking-DGB configuration [7]. This yields a 4% scale of the vent area, disk and band dimensions, geometric porosity, suspension-line length, trailing distance, etc. Because of

Table 1 4%-scale DGB constrained parachute test matrix [6]

Test	Mach	Re $(\times 10^5)$	q, kPa	Trim, deg	d/D_o	D_o, m	x/d
1	2	0.77	17.4	0	0.21	0.813	10.6
2	2.2	1.03	18.6	0	0.21	0.813	10.6
3	2.5	1.29	19.9	0	0.21	0.813	10.6

Table 2 Subscale and full-scale parameters.

Parameter	Subscale	MSL
Nominal diameter D_o	0.813 m	21.5 m
Projected diameter D_o	0.67 D_o	0.67 D_o
Number of gores	24	80
Entry-vehicle nominal diameter	0.21	0.21
Suspension-line length	1.7D_o	1.7D_o
Suspension-line thickness/ D_o	0.0012	0.0002
Suspension-line Young's modulus, GPa	43.0	12.9
Canopy-fabric Young's modulus, GPa	0.88	0.69
Max Reynolds number Re	1.3×10^6	1.0×10^6
Mass ratio $m_p/\rho D_o^3$	2	10
Max dynamic pressure, Pa	20×10^3	750
Trailing distance x/d	10.6	10.4

construction limitations and to minimize the effects of suspension-line shock and wake generation, the number of gores is not identical to full scale. As mentioned previously, to provide the flight Reynolds number, significantly higher dynamic pressure is needed in the subscale wind-tunnel test. A 20 kPa dynamic pressure deployment necessitated the use of 1.15 oz/yd^2 of nylon and suspension lines that were six times thicker than the flight article, when normalized by D_o. The material scaling differences result in a factor of 3.3 and 1.3 times stiffer than the full-scale article for the canopy fabric and suspension lines, respectively. The increased stiffness results in a more scalloped-band leading-edge profile, as compared with the full-scale inflated shape. The effect on the parachute's dynamic response to the flowfield is second order for the nondimensional mass ratio associated with the full and subscale flight regimes [19]. Thicker suspension lines have a significant effect on performance, both increasing geometric blockage in the vent region and generating shocks capable of altering the subsonic wake's coupling to the parachute. These subjects are discussed in greater detail in Sec. IV. Reference [20] has greater detail on the parachute design.
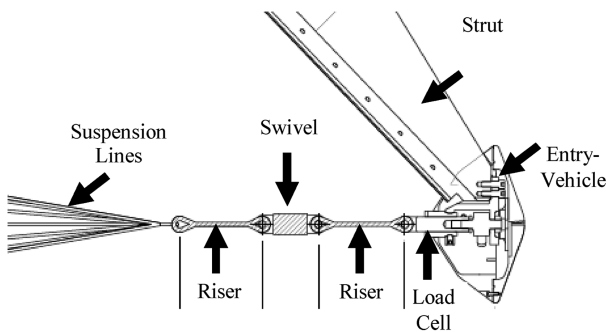

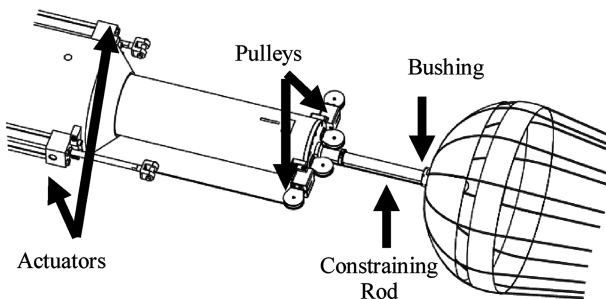**Fig. 2 The entry-vehicle-to-parachute connection.**

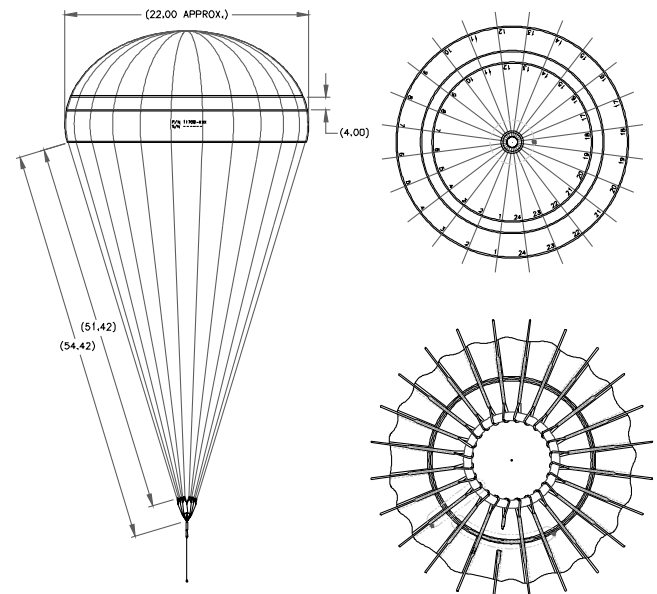**Fig. 3 Schematic of the constrained parachute and deployment system.**

Fig. 4 Schematic showing (left) side view and (upper right) top down view and (lower right) detail of the vent region of the 0.813 m parachute.
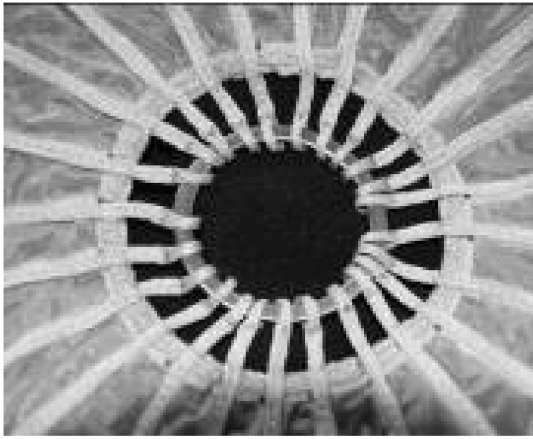
Fig. 7 Photo of the parachute rigged in the deployment sleeve showing ripcord, lazy leg, and mouth termination pin.

actuated on command, as shown in Fig. 7. The sleeve was designed to unlace from apex to leading edge, ensuring separation of the sleeve before the onset of parachute inflation to mitigate the potential for friction burning. The sleeve deployment was triggered by a hydraulic actuator that severed a breakline to which the ripcord was attached. The ripcord was secured to the sleeve via Teflon pull-pins that were inserted through Spectra loops on either side of the sleeve seam. The termination of the ripcord was a pull-pin that closed off the mouth of the parachute, as shown in Fig. 7. A bungee loop was used to provide sufficient force and stroke to pull the ripcord after the breakcord was severed by the actuator, as shown in Fig. 8. The bungee was tensioned by the same actuator as the breakcord. A lazy leg was also attached to the downstream end of the sleeve and bungee. It was sized such that following removal of the ripcord the remaining bungee force would pull on the lazy leg, causing it to pull the sleeve away from the canopy. This eliminated any potential interaction between the inflating parachute and sleeve.

C. Diagnostics

Flowfield measurements were made with nonintrusive diagnostics to minimize interference with the wake structure and its interaction with the parachute. A shadowgraph of the parachute bow-shock region was obtained via optical windows on either side of the test article, as shown in Fig. 1. Images were collected from 2000 to 4000 frames/second to resolve the frequency and the parachute bow-shock oscillation. The video data yield mean and rms bow-shock shape and standoff distance as well as the frequency of oscillation. Shadowgraph data were also collected during inflation on some runs.

Drag was measured with a single-axis load cell mounted within the entry vehicle. Force was measured from the parachute single riser through the swivel in the freestream flow direction. Data were collected at 20 kHz. Drag was calculated in the same method as the Viking-era wind-tunnel programs, for consistency [21].

$$C_D = \frac{F_D}{q\frac{1}{4}\pi D_o^2}$$

Dynamic pressure was not adjusted to account for tunnel-blockage effects, to be consistent with the method in [21]. Tunnel blockage tends to drive up the effective dynamic pressure in the vicinity of the parachute and reduce the measured drag coefficient.

High-speed pressure transducers and static pressure ports were also placed on the entry-vehicle backshell to provide mean and rms pressures at known point locations. The transducers used the reference static ports to define the absolute pressure.

High-speed-video data were collected for both imaging and photogrammetric measurement purposes. A total of four camera views were used (left side, right side, top, and bottom), focused downstream on the canopy's interior, looking downstream. The cameras were operated from 1000 to 4000 frames/second, depending on the data required. Subsequent testing revealed 2000 frames/second were needed to resolve the canopy motion postinflation for the photogrammetric postprocessing technique.

Stereo PIV was used to measure the three components of velocity in the parachute bow-shock region over an axial plane centered in the tunnel, from the $x/d = 6$ to 10 position. Figure 9 shows the PIV configuration and location of the laser light sheet relative to the parachute and entry vehicle. The stereo PIV system employed high-resolution cameras (4000×2672 pixels) to provide high-spatial-resolution velocity measurements (2.5 ± 0.1 mm) over a large field of view (400×700 mm) [22]. PIV images were recorded at 2 Hz for

Fig. 5 Photograph of the apex region of the constrained parachute showing vent ring and vent line terminations (top) and CAD drawing of vent bushing in the disassembled configuration (bottom).

The constrained parachutes have the added feature of a stainless steel vent ring that was sewn into the apex of the canopy, as shown in Fig. 5. Each vent line terminates at the ring around which a two-piece bushing was installed. The bushing has a smooth bore interior, allowing minimal frictional resistance as the parachute travels along the length of the constraining-rod, and is shown in Fig. 5 as well. The constraining rod was sized to allow for free upstream and downstream translations of the parachute. A hemispherical end cap was placed on the upstream end of the rod to prevent the parachute apex from coming off. To account for geometric vent blockage caused by the thickness of the rod, vent ring, and vent line, the vent diameter of the parachutes was increased. The effective open area was equivalent to the Viking-scaled vent area.

Deployment of the parachutes in a supersonic wind-tunnel environment was a significant challenge. The startup environment of the wind tunnel is characterized by turbulent and separated subsonic flow before the passage of the shock. It was determined that the parachutes would not survive the startup flow environment, necessitating the implementation of a stowage and deployment mechanism to protect the parachute before passage of the shock. The deployment method selected was a Spectra deployment sleeve, as shown in Fig. 6. The sleeve unlaces by means of a break-tied daisy-chain cord
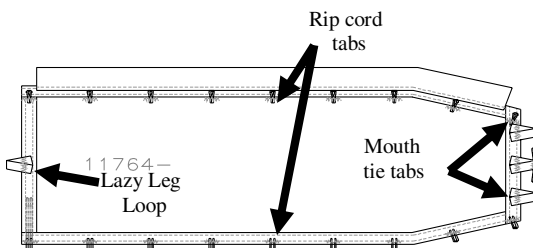

Fig. 6 Schematic of the deployment sleeve in the unlaced configuration. The smaller tabs along the length are for the ripcord installation. A mouth tie is fed through the upstream tabs to prevent airflow into the canopy.

5 to 10 min, providing 600 to 1200 instantaneous measurements of the velocity field in this region. The processed PIV data include mean 3-component velocity, 3-component rms velocity, and turbulence statistics. The mean and rms bow-shock shape, standoff distance, and frequency were also obtained. Knowledge of the time stamp of each instantaneous measurement allows reconstruction of the periodic and oscillatory motions [22].

An Inter-Range Instrumentation Group (IRIG) time code was included with each data point and/or image frame, allowing time synchronization between the diagnostics employed. The IRIG time stamp had a carrier resolution of 10 kHz and pulse frequency of 1 ms.

III. Experimental Results

The experimental results include a description of the 0 deg constrained canopy motion and fabric dynamics from high-speed video, mean and unsteady drag data, and shadowgraph and PIV of the flowfield. Digital image postprocessing was used to reduce the area oscillation frequency, projected area variation during the instability, inflation time, bow-shock oscillation frequency, and bow-shock standoff-distance variation. PIV data reduction is underway and will be presented in another publication [23].

A. Parachute Dynamics

The parachute fabric dynamics were characterized by periodic infolds in the band region at times leading to canopy collapse and subsequent reinflation events. The frequency associated with the infolding was determined from high-speed imaging. The frequency of the motion increased with Mach numbers from 2 to 2.5. The collapse and reinflation events were characterized as area oscillations. The behavior is consistent with previous observations of the phenomena in the Viking and pre-Viking supersonic flight and wind-tunnel programs. Area oscillations occurred at all three Mach numbers investigated. A representative oscillation at each Mach number tested is shown in Fig. 10. The collapse event was observed to propagate from the band leading edge inward toward the center of the canopy. The area oscillations were also characterized by the projected area variation and frequency associated with the collapse and subsequent reinflation. These parameters were reduced from the digital images of each frame of the high-speed video during an oscillation event. The projected area variation A_p was observed to increase with Mach number and ranged from 46 to 68% ($\pm10\%$) of full open during an oscillation event from Mach 2 to 2.5, respectively. It is important to note that the onset of an oscillation appeared to be random; however, once an oscillation occurred, it was followed by two to five subsequent collapses and reinflation events, with a consistent time interval period between each. It is important to point out that area oscillations occurred throughout the test interval with a frequency ω_{AO} between 70 and 90 Hz (±10 Hz) for Mach 2.0 to 2.5 during the event. Parameters reduced from the video data analysis are summarized in Table 3.

B. Drag Performance

The measured normal force was used to compute the drag coefficient. Nonaxial drag was not measured or included in the computation of drag, as the parachute was constrained to the axis. The drag coefficient versus Mach number is plotted in Fig. 11. The trend of decreasing C_D with Mach number is evident in the data set. Also included in the figure are data obtained from the pre-Viking supersonic wind-tunnel program of unconstrained subscale parachutes [21]. The measurements are comparable with the Viking subscale data set, over the same Mach number range. It is important
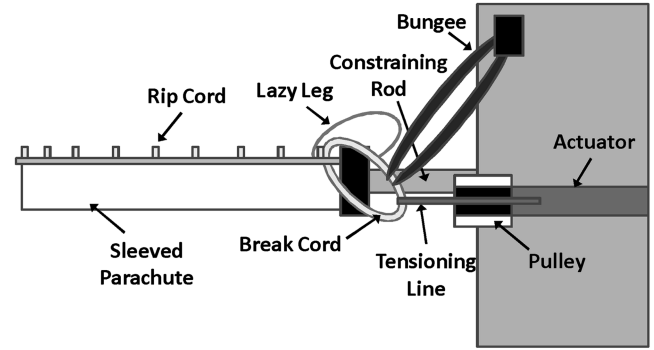

Fig. 8 Schematic of the parachute in the deployment sleeve showing textile connections. Following breakage of the breakcord the energy stored in the bungee pulls out the ripcord and deploys the parachute.
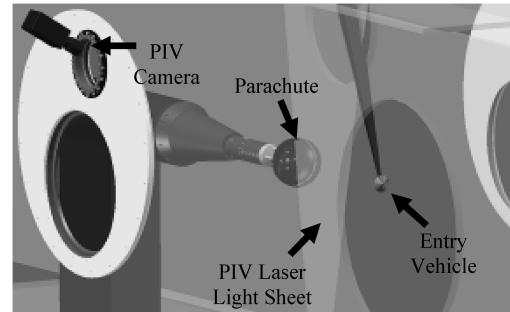

Fig. 9 PIV data plane in the tunnel. The flow direction is from right to left.

to note that tunnel-blockage and trailing-distance effects were not included in the calculation of drag. This was done to provide consistency with measured drag from [21]. Qualitatively, tunnel blockage for the Viking data set was higher than for MSL, which would tend to bring the two data sets closer together in terms of effective drag coefficient. However, the Viking data were from parachutes with an $x/d = 8.5$ at a lower dynamic pressure, which could reduce the drag coefficient. As these parameters are not well understood in the supersonic environment, an adjustment for these factors has not been attempted.

The rms drag is plotted against nondimensional inflation time t^* in Fig. 12. Time is nondimensionalized by the time from deployment to full inflation (t_{FI}) for each of the Mach number investigated. The t_{FI} for the Mach numbers investigated is shown in Table 3. The rms drag varied by as much as 2.25 times the mean value. The rms drag also indicates two dominant frequencies. It is likely that the higher-frequency component was driven by the bow-shock oscillation and the lower-frequency component was driven by the area oscillation instability. Another interesting finding from the rms drag is that the peak drag load did not coincide solely with the initial inflation opening shock. Instead, subsequent reinflations during the area oscillation instability were characterized by peak loads within 2% of the initial inflation load. In a free-flight application, the parachute will decelerate the entry vehicle and reduce the peak load from that of the initial inflation load. But from a structural loading perspective, this does suggest that the parachute will see a dynamic load factor similar to that of an opening shock augmentation. This presents difficulties in the traditional subsonic qualification of a supersonic parachute, as a single load application does not represent the flight environment.

C. Shadowgraph

Shadowgraph imaging provided insight into the flowfield upstream of the parachute. The parachute bow-shock shape and standoff distance varied in a cyclical fashion consistent with the unsteady parachute response and drag performance. Figure 13 is an image of the bow shock at Mach 2 and 2.5. The bow shock varied

Table 3 Parachute video data analysis

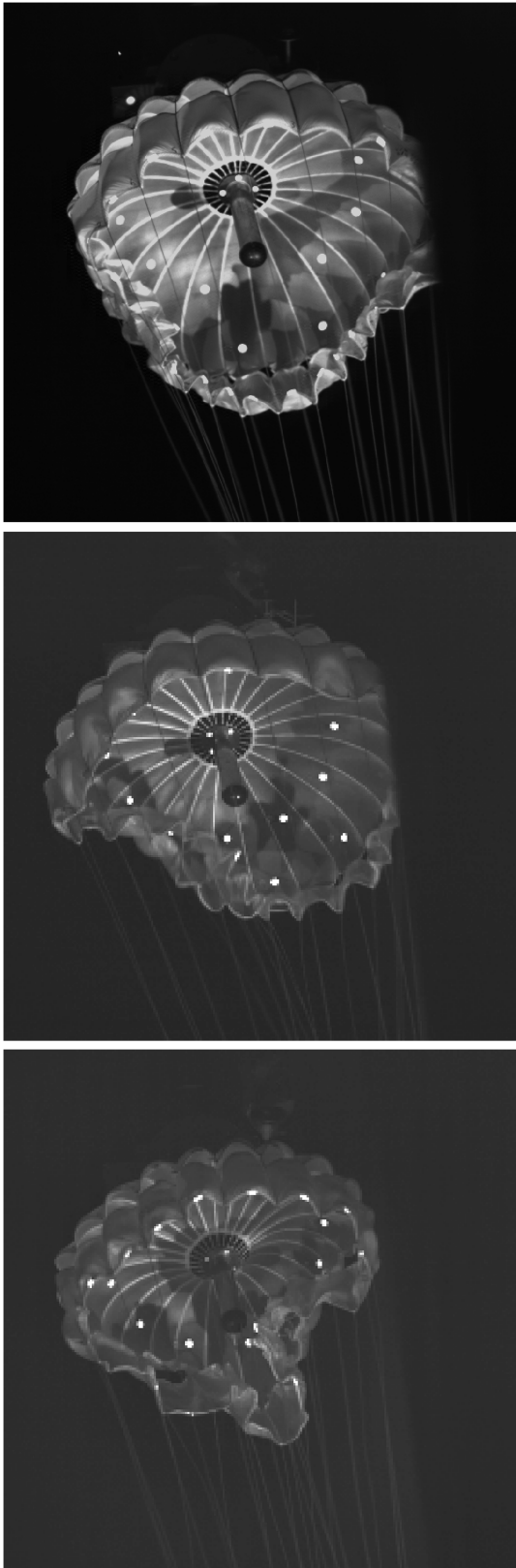| Test	Mach	ω_{AO}, Hz	t_{FI}, ms	$A_{p,\min}$, %
1	2	70	12.4	68
2	2.2	81	11.5	52
3	2.5	90	10.9	46

Fig. 10 Area oscillation at (top) Mach 2.0, (middle) Mach 2.2 and (bottom) Mach 2.5 for a 0 deg constrained 0.813 m DGB parachute.
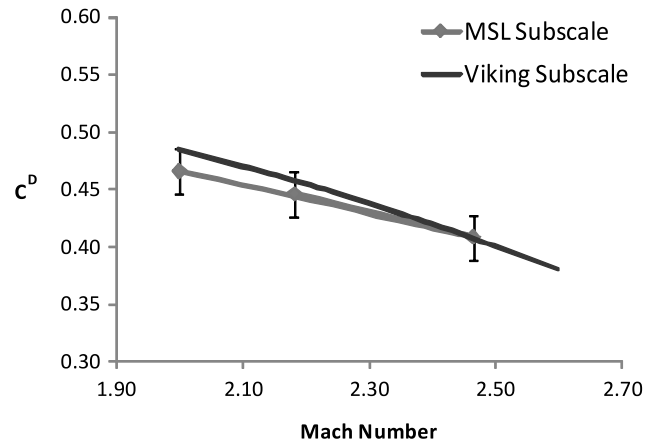

Fig. 11 Measured drag coefficient for the MSL subscale of 0 deg constrained plotted with Viking subscale.

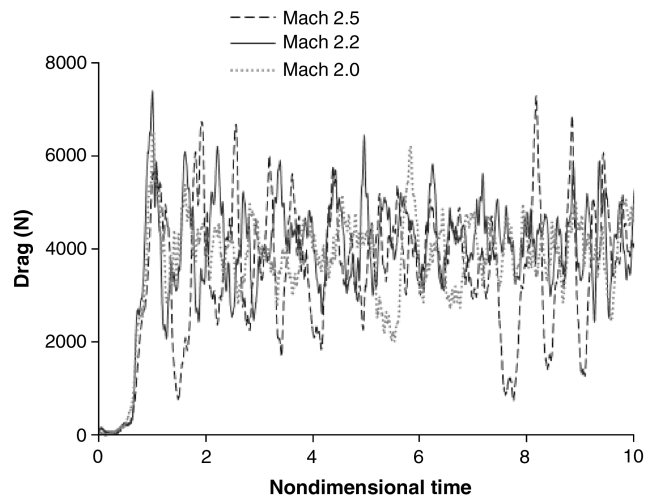**Fig. 12 RMS drag variation from Mach 2 to 2.5.**

from conical to detached and the parachute responded in kind for all Mach numbers investigated. The detached bow-shock state was related to nominal inflation. During this variation the pressure distribution in the canopy varied, as evidenced by changes in the parachute's inflated shape (projected area). The extreme conical shock state was related to band infolding. This suggests a pressurization and depressurization of the parachute interior determined

by the bow shock. Testing and computational fluid dynamics simulations of a rigid DGB parachute configuration exhibited a similar bow-shock shape variation in a cyclical manner, suggesting that the physical mechanism driving the instability is aerodynamic [15,18,22].

The flowfield during an area oscillation is shown in Fig. 14 for Mach 2.0 and 2.5. The shadowgraph images shown were taken during the most collapsed state of the canopy during the oscillation. Compared with the fully inflated state, the shock is more conical, attached, and skewed by the collapsed state of the parachute mouth. The time-resolved shadowgraph imaging suggests a transition toward a shock ingestion; however, this never occurred and the canopy instead reinflates and pushes the shock back upstream.

Several other features from the shadowgraph imaging are worthy of discussion. In the fully inflated state, the bow shock was asymmetric, which can be attributed to the strut contribution to the wake. At times, a pressure discontinuity or contact surface at the canopy mouth was observed, possibly established by mass flow into and out of the canopy. At times, suspension-line shocks were observed to disrupt the parachute bow shock. This coincided with more violent fabric dynamics and will be discussed in the following section.

IV. Discussion

A. Mach and Reynolds Number Dependence

There is a clear Mach dependence of all parameters measured from Mach 2 to 2.5. Drag coefficient decreases with Mach numbers from 2 to 2.5. Similarly, increasing the Mach number also increased the
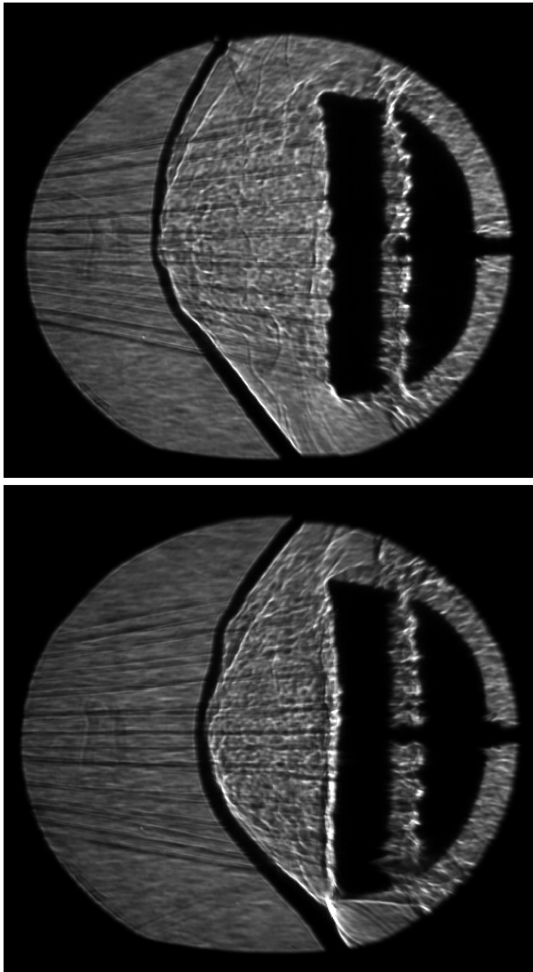
Fig. 13   Shadowgraph of bow shock when parachute is fully inflated (top) Mach 2.0 and (bottom) Mach 2.5.
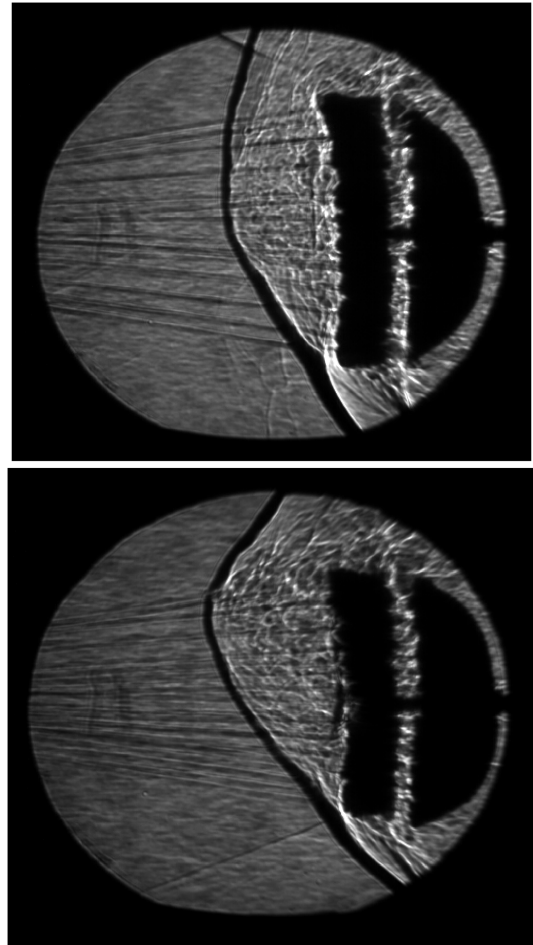

Fig. 14   Shadowgraph of an area oscillation at (top) Mach 2.0 and (bottom) Mach 2.5. These images correspond to the most collapsed state of the canopy during the area oscillation event.

parachute lateral and inflation stability. Shadowgraph data supports this trend as well. The parachute bow-shock morphology was more chaotic with increasing Mach number, resulting in more violent fabric dynamics. Such responses to higher Mach affect parachute performance and should be factored into the overall EDL performance. The supersonic environment also has implications to structural margin and durability, as a dynamic/oscillatory flow environment fatigues the canopy and increases the abrasion between loaded textile members.

B.   Suspension-Line Interaction

Table 2 lists the ratio of suspension-line thickness to parachute nominal diameter for the full scale and 4%-scale parachute. The subscale parachute lines are 6.5 times thicker and occupy 47 times the area, as compared with the full-scale parachute. Therefore, any suspension-line effects will be more pronounced in the subscale configuration as compared with actual flight. Figure 15 is an image of the bow-shock region of the parachute to illustrate this effect. Shocks from the suspension lines create large-density disturbances that at times disrupt the parachute bow shock in the shadowgraph video. The response of the parachute to this disruption was a partial collapse of the canopy (i.e., an area oscillation). As most oscillation events were not captured by shadowgraph at this time, we can only conclude that suspension-line shocks exacerbate area oscillations. Future testing will be done to determine if they in fact trigger the supersonic instability. This is relevant because the original Viking parachutes used Dacron suspension lines with a thickness-to-nominal-diameter ratio of 0.00157, similar to that of the subscale test article [11]. We can expect this effect to be reduced with modern parachutes, as Kevlar has a higher strength-to-weight ratio than Dacron, resulting in

proportionately thinner suspension lines. Therefore, the non-dimensionalized frequency of area oscillations in the subscale test environment is a conservative representation of parachute performance on Mars.

C.   Supersonic Inflation

High-speed video and shadowgraph of the initial supersonic parachute inflation was obtained. Inflation time is defined as sleeve
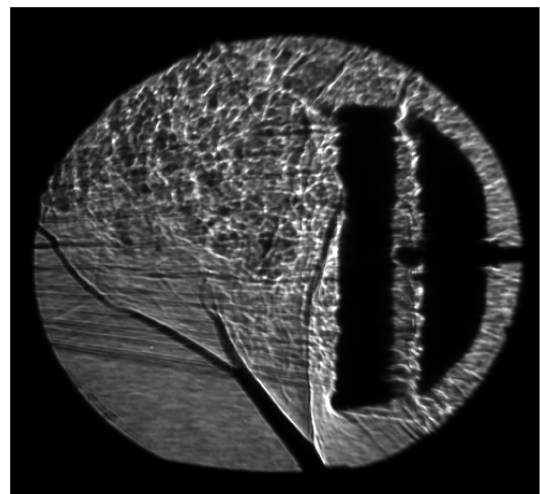

Fig. 15   Suspension-line interaction and bow-shock disruption at Mach 2.0.
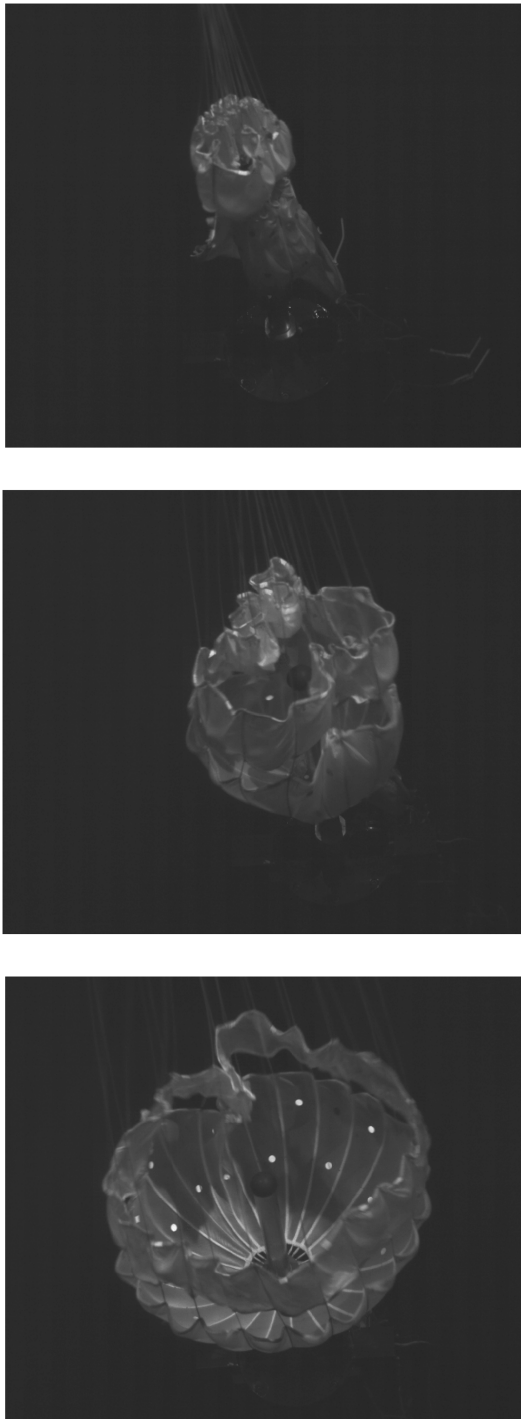
Fig. 16 Images of supersonic initial inflation at Mach 2.5. The images document, left to right, 2, 4, and 6 ms from sleeve release (deployment).

release to first full open. Observed times ranged from 11 to 14.5 ms (± 0.25 ms) for the 0 deg parachutes. The sleeve deployment differs from a mortar deployment due to the absence of bag-stripping forces and the absence of momentum of the pack providing tensioning to the lines. Nevertheless, the sleeve deployment does provide an accurate presentation of the skirt presentation to the wind stream and canopy-filling dynamics at line stretch in a supersonic environment immediately following bag strip. Figure 16 shows the parachute from 2 to 5.5 ms into its initial supersonic inflation. The parachute unfurled from its flaked configuration in an orderly fashion. The final three to five gores appeared to experience an infold, but this presentation is consistent with the Planetary Entry Parachute Program 19.7 m parachute inflation video. At 4 ms into the inflation, the canopy presentation is similar to that of an area oscillation event. This shape

does not present an unstable state for the parachute. It is also important to point out that flag drag and flapping dynamics were not observed during the inflations. The supersonic fill-time constant was quite short, preventing these common subsonic modes from appearing before a fully inflated condition. It should also be noted that area oscillations did not occur before full open.

V. Conclusions

A series of wind-tunnel experiments were performed to determine the supersonic performance of a subscale representation of the MSL DGB parachute in the wake of a sphere-cone biconic entry vehicle. The Mach and Reynolds number dependence of the parachute's performance was investigated with nonintrusive diagnostic techniques. Shadowgraph, in conjunction with high-speed video, revealed that canopy-fabric dynamics are caused by variations in the shape and standoff distance of the parachute bow shock and suspension-line interaction. The magnitude and frequency of this variation was a function of Mach number and Reynolds number. The shape change corresponded to pressurization and depressurization of the canopy, resulting in periodic fabric motion and, in some instances, large projected area fluctuations. The majority of the canopy motion was band oscillation with leading-edge infolds. However, the supersonic instabilities referred to as area oscillations were observed and documented with shadowgraph and high-speed video. They occur when the bow shock is disrupted and were more prevalent with increasing Mach number and Reynolds number. A critical finding is the effect suspension-line shocks have on parachute supersonic stability. Specifically, area oscillations are exacerbated by suspension-line interaction with the conical shock.

Another critical data set obtained from the test was high-resolution video of supersonic DGB parachute inflation. Video of the inflating parachutes revealed a consistent and orderly unfurling on the canopy from its rigged state. The canopies did not have any difficulty in inflated or anomalous opening behavior. Inflation occurred in less than 15 ms for all Mach numbers tested. The parachute also appeared to inflate from the mouth and followed an orderly unfurling from its rigged condition.

The parachute drag performance was consistent with prior Viking subscale DGB parachutes tested from Mach 2.0 to 2.5. Therefore, changes to the existing MSL Mach efficiency curve are not required. Dynamic parachute drag data revealed two dominant frequencies: one associated with bow-shock oscillation due to canopy wake coupling and another associated with the area oscillation event. These frequencies increased with Mach numbers from 2.0 to 2.5.

In summary, the area oscillation phenomenon was observed and quantified in the experimental studies performed on a 0.8 m DGB parachute. The results suggest that nondimensional aerodynamics parameters and geometric scaling are valid in understanding the physics of supersonic parachute operation on Mars.

References

[1] Way, D., Powell, R., Chen, A., and Steltzner, A., "Asymptotic Parachute Performance Sensitivity," 2006 IEEE Aerospace Conference, Big Sky, MT, Inst. of Electrical and Electronics Engineers Paper IEEEAC 1465, March 2006.

[2] Mitcheltree, R., Lee, W., Steltzner, A., and SanMartin, A., "Mars Exploration Rover Mission: Entry, Descent, and Landing System Validation," International Astronautical Federation, Paper IAC-04-Q.3.a.02, Oct. 2004.

[3] Hoffman, P., Rivellini, T., Slimko, E., Dahya, N., Agajanian, A., Knight, J., Sengupta, A., Thoma, B., Webster, R., Gallon, J., Gradziel, M., "Preliminary Design of the Cruise, Entry, Descent, and Landing Mechanical Subsystem for MSL," IEEE Aerospace Conference, Big Sky, MT, Inst. of Electrical and Electronics Engineers, March 2007, pp. 1–18.

[4] Mitcheltree, R., Steltzner, A., Chen, A., SanMartin, M., and Rivellini, T., "Mars Science Laboratory Entry Descent and Landing System Verification and Validation Program," *2006 IEEE Aerospace Conference*, Inst. of Electrical and Electronics Engineers, Piscataway, NJ, 2006.
doi:10.1109/AERO.2006.1655799.

[5] Steltzner, A., Kipp, D., Chen, A., Burkhart, P., Guernsey, C., Mendeck, G., Mitcheltree, R., Powell, R., Rivellini, T., San Martin, M., Way, D., "Mars Science Laboratory Entry, Descent, and Landing System," 2006 IEEE Aerospace Conference, Big Sky, MT, Inst. of Electrical and Electronics Engineers, Paper 1497, March 2006.

[6] Ingoldby, R. N., Michel, F. C., Flaherty, T. M., Dory, M. G., Preston, B., Villyard, K. W., and Steele, R. D., "Entry Data Analysis for Viking Landers 1 and 2," NASA, CR 159388, Nov. 1976.

[7] Dickenson, D., Schlemmer, J., Hicks, F., Michel, F., and Moog, R., "Balloon Launched Decelerator Test Post-Flight Test Report BLDT Vehicle AV1," NASA TR-3720289, Sept. 1972.

[8] Dickenson, D., et al., "Balloon Launched Decelerator Test Post-Flight Test Report BLDT Vehicle AV4," NASA TR-3720295, Oct. 1972.

[9] Moog, R. D., and Michel, F. C., "BLDT Summary Report," NASA TR-372039, March 1973.

[10] Sengupta, A., Steltzner, A., Witkowski, A., and Rowan, J., "An Overview of the Mars Science Laboratory Parachute Decelerator System," Inst. of Electrical and Electronics Engineers, Paper 1432-2007, March 2007.

[11] Murrow, H., and McFall, J., "Some Test Results from the NASA Planetary Entry Parachute Program," *Journal of Spacecraft and Rockets*, Vol. 6, No. 5, 1969, pp. 621–623.
doi:10.2514/3.29624

[12] Reichenau, D. E., "Aerodynamic Characteristics of Disk-Gap-Band Parachutes in the Wake of Viking Entry Forebodies at Mach Numbers from 0.2 to 2.6," Arnold Engineering Development Center, TR-72-78, Arnold AFB, TN, 1972.

[13] Couch, L., "Drag and Stability Characteristics of a Variety of Reefed and Un-Reefed Parachute Configurations at Mach 1.8 with an Empirical Correlation for Supersonic Mach Numbers," NASA TR R-429, Feb. 1975.

[14] Sengupta, A., et al., "Results from the Mars Science Laboratory Parachute Decelerator System Supersonic Qualification Program," Inst. of Electrical and Electronics Engineers, Paper 1435-2008, March 2008.

[15] Barnhardt, M., Drayna, T., Ioannis Nompelis, Candler, G. V., and Garrard, W., "Detached Eddy Simulations of the MSL Parachute at Supersonic Conditions," AIAA Paper 2529-2007, May 2007.

[16] "10- by 10-Foot Supersonic Wind Tunnel," NASA Rept. TOP3-00226, Jan. 2007; available online at http://facilities.grc.nasa.gov/documents/TOPS/Top10x10.pdf [retrieved June 2009].

[17] Equist, K., Hollis, B., Dyakonov, A., Laub, B., Wright, M., Rivellini, T., Slimko, E., and Willcockson, W., "Mars Science Laboratory Entry Capsule Aerothermodynamics and Thermal Protection System," Inst. of Electrical and Electronics Engineers, Paper 1423-2007, March 2007.

[18] Gidzak, V., Barnhardt, M., Drayna, T., Nompelis, I., Candler, G., and Garrard, W., "Simulation of fluid–structure Interaction of the Mars Science Laboratory Parachute," AIAA Paper 2008-6910, Aug. 2008.

[19] Niemi, E., "An Improved Canopy Stiffness Scaling Law for Determining Opening Time of Flat Circular Parachutes," AIAA Paper 90-3058, 1990.

[20] Witkowski, A., Kandis, M., Reuter, J., Machalic, W., Kelsch, R., and Sengupta, A., "Design of Subscale Parachute Models for MSL Supersonic Wind Tunnel Testing," 20th AIAA Aerodynamic Decelerator Systems Technology Conference, Seattle WA, AIAA Paper 2009-2999, May 2009.

[21] Jaremenko, I., Steinberg, S., and Faye-Petersen, R., "Scale Model Test Results of the Viking Parachute System at Mach Numbers from 0.1 Through 2.6," NASA TR-3720181, Nov. 1971.

[22] Sengupta, A., Steltzner, A., Comeaux, K., Candler, G., Pantano, C., Bell, J., "Supersonic Delta Qualification by Analysis Program for the Mars Science Laboratory Parachute Decelerator System," AIAA Paper 2007-2542, May 2007.

[23] Wernet, M. P., Lock, R. J., and Wroblewski, A., "Application of Stereo PIV on a Supersonic Parachute Model," 28th AIAA Aerospace Sciences Conference, Orlando, FL, AIAA Paper 2009-70, Jan. 2009.

M. Miller
Associate Editor